

# Occlusion-Resistant LiDAR Fiducial Marker Detection

Yibo Liu, Jinjun Shan, Hunter Schofield

**Abstract**—The LiDAR fiducial marker, akin to the well-known AprilTag used in camera applications, serves as a convenient resource to impart artificial features to the LiDAR sensor, facilitating robotics applications. Unfortunately, current LiDAR fiducial marker detection methods are limited to occlusion-free point clouds. In this work, we present a novel approach for occlusion-resistant LiDAR fiducial marker detection. We first extract 3D points potentially corresponding to the markers, leveraging the 3D intensity gradients. Afterward, we analyze the 3D spatial distribution of the extracted points through clustering. Subsequently, we determine the potential marker locations by examining the geometric characteristics of these clusters. We then successively transfer the 3D points that fall within the candidate locations from the raw point cloud onto a designed intermediate plane. Finally, using the intermediate plane, we validate each location for the presence of a fiducial marker and compute the marker’s pose if found. We conduct both qualitative and quantitative experiments to demonstrate that our approach is the first LiDAR fiducial marker detection method applicable to point clouds with occlusion while achieving better accuracy.

## I. INTRODUCTION

The visual fiducial marker, such as AprilTag [1], ArUco [2], and CCTag [3], have been widely utilized in many robotic applications, including SLAM [4], [5], multi-sensor calibration [6], autonomous navigation [7], [8], [9], [10], object tracking [11], [12], and Augmented Reality (AR) [13] as they can provide artificial features (a.k.a. fiducials) for the camera.

The development of the LiDAR fiducial marker is also crucial, as it fulfills fundamental needs for feature extraction and matching in diverse LiDAR applications [14], [15], [16]. However, detecting LiDAR fiducials is a challenging task since the 3D point cloud is unordered and sparse compared to a camera image [17]. While there have been some pioneering LiDAR fiducial marker detection methods, they require an occlusion-free point cloud as input, making them incapable of handling the fiducial marker detection problem in a scenario depicted in Fig. 1. Resolving this problem is favorable to downstream tasks, such as relocalization [18] and navigation [7], [19].

To this end, we develop an occlusion-resistant LiDAR fiducial marker detection method in this work. In particular, our method first conducts downsampling on the raw point

cloud using the 3D intensity gradients to locate objects with high-intensity contrast. Then, we cluster the intensity features and analyze whether a cluster is a potential fiducial marker from a geometric perspective, according to the characteristics of a planar marker. Finally, we check whether each preserved location of the raw point cloud contains a fiducial marker through a designed intermediate plane and calculate the pose if found. We carry out experiments on both synthetic and real-world scenes against the state-of-the-art methods to demonstrate that our method is the first LiDAR fiducial marker detection method capable of dealing with point clouds with occlusion while achieving better accuracy.

The main **contributions** of this work are as follows:

- We propose a novel LiDAR fiducial marker detection method specifically for point clouds with occlusion, which is a problem that cannot be resolved by the existing approaches [20], [17], [21].
- We design a new feature extraction pipeline that jointly leverages both 3D intensity features and 3D geometric features, considering that fiducial markers are planar objects with high-intensity contrast and are non-distinguishable from the plane to which they are attached. This differs from conventional 3D object detection methods [22], [23], [24], [25], [26], [27] that rely solely on 3D geometric features and can only detect spatially distinguishable objects.
- We conduct thorough experiments qualitatively and quantitatively to demonstrate the superiority of our approach over the existing methods [20], [21], [17]. Moreover, we release the open-source implementation based on C++ to the community.

## II. RELATED WORK

**3D Object Detection.** 3D object detection methods can be categorized into two groups: conventional approaches [22], [23], [24], [25], [26] and deep-learning-based approaches [27], [31], [32], [33], [34]. The conventional methods utilize mathematical and geometric methods to segment 3D objects from the scene, including edge-based [22], region-based [23], attributes-based [24], model-based [25], and graph-based [26] methods. The deep-learning-based approaches [27], [31], [32], [33], [34] adopt elaborately designed neural networks to detect specific 3D objects, such as vehicles, pedestrians, desks, chairs, etc. These methods rely on the assumption that objects are spatially distinguishable from each other, which means they cannot effectively detect objects that lack such spatial distinction. For instance, detecting a thin sheet of paper attached to a wall poses a challenge for these approaches.

This work was supported in part by NSERC Alliance Program under Grant ALLRP 555847-20, and in part by Mitacs Accelerate Program under Grant IT26108.

The authors are with Department of Earth and Space Science and Engineering, York University, Toronto, Ontario M3J 1P3, Canada {yorklyb, jjshan, hunterls}@yorku.ca

The open-source implementation of this work is available at: <https://github.com/York-SDCNLab/Marker-Detection-General>.

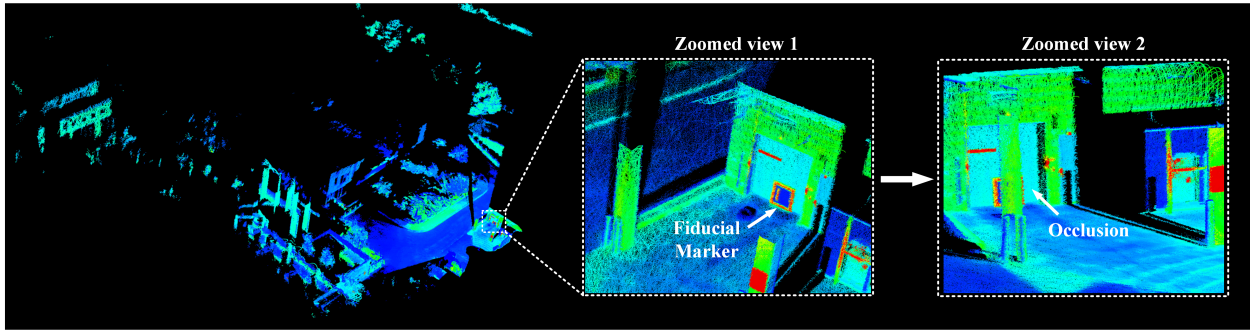


Fig. 1. An example of a point cloud with occlusion. The points are rendered by intensity values through the color map [28]. The point cloud is generated by the modified *livox-mapping* SLAM framework [29], [30]. As shown in the zoomed view 1, there is an ArUco marker [2] (family: original; ID: 0) placed in front of the shutter door. As seen in the zoomed view 2, occlusion exists seeing from the origin of the point cloud towards the fiducial marker.

**LiDAR Fiducial Marker Detection.** LiDAR fiducial marker is inherently a 3D object. Therefore, LiDARtag [17] and A4LiDARtag [21] follow conventional 3D object detection methods [22], [26] to develop fiducial markers for LiDAR sensors. However, to guarantee that fiducial markers have spatial distinction, their fiducial markers have to be additional 3D objects added to the environment. In contrast, the Intensity Image-based LiDAR Fiducial Marker (IILFM) [20] proposes to utilize the intensity image and an embedded 2D marker detector to localize LiDAR fiducial markers. Thus, adding a marker does not affect the 3D environment, as the marker is simply a thin sheet of paper attached to a plane. In this work, LiDAR fiducial marker refers to this type of marker. Furthermore, a few works [35], [36], [37] adopt high-reflectivity targets as fiducials for LiDAR-camera calibration purposes. These approaches cannot assign each fiducial a unique identification number, as is done with the AprilTag [1], LiDARtag [17], and IILFM [20]. Despite the proposal of the aforementioned methods [17], [20], [21], LiDAR fiducial marker detection in a point cloud with occlusion remains an unresolved problem as they all require an occlusion-free single-view point cloud as the input.

### III. METHODOLOGY

#### A. Preliminaries

In this work, we aim for the LiDAR fiducial markers to be sheets of thin paper and not to affect the 3D environment, akin to the IILFM [20]. Thus, we choose IILFM as the baseline model. In this section, we introduce preliminaries regarding IILFM to further explain why occlusion is a fatal hindrance in this method.

IILFM first projects the 3D points of the raw point cloud into a 2D image plane to construct the intensity image and then adopts the 2D marker detector to find 2D fiducials on it. Finally, the detected 2D fiducials are projected back into 3D space. In particular, the intensity image is generated by transforming each 3D point in the raw point cloud into a 2D pixel on an image plane:

$$u = \lceil \frac{\theta}{\Theta_a} \rceil + u_o, v = \lceil \frac{\phi}{\Theta_i} \rceil + v_o \quad (1)$$

where  $[u, v]^T$  are the image coordinates of the projected pixel.  $[\theta, \phi, r]^T$  are the spherical coordinates of the 3D point.  $\Theta_a$  and  $\Theta_i$  are the angular resolutions in  $u$  (azimuth) and  $v$  (inclination) directions, respectively.  $u_o$  and  $v_o$  are the offsets. Apparently, for any two points sharing the same  $[\theta, \phi]^T$ , they will overlap for the same pixel. This indicates that occlusion ruins the intensity image due to pixels overlapping.

#### B. Downsampling Based on 3D Intensity Gradients

As declared above, the fiducial markers in this work refer to sheets of thin paper that are not spatially distinguishable from the attached planes. Thus, it is infeasible to adopt previous geometric features-based 3D object detection methods [22], [23], [24], [25], [26], [27], [31], [32], [33], [34] to find the fiducial markers.

Despite this, a fiducial marker is composed of a black-and-white pattern and, as a result, presents as a high-intensity contrast object in the view of a LiDAR (see the zoomed view 1 of Fig. 1). This indicates that we can first analyze the point cloud from the intensity perspective. In particular, we conduct downsampling on the raw point cloud based on the 3D intensity gradients. We take the intensity as a function  $I(\mathbf{x})$  of the 3D coordinates  $\mathbf{x} = [x, y, z]^T$ . Suppose that the given 3D point/location is  $\mathbf{p}_0$ , we define the point set composed of the neighbouring  $n$  points around  $\mathbf{p}_0$  as  $\mathcal{P}_I = \{\mathbf{p}_1, \mathbf{p}_2, \dots, \mathbf{p}_n\}$ . In practice, we use a linear model,  $\hat{I}(\mathbf{x})$ , to approximate  $I(\mathbf{x})$ :

$$\hat{I}(\mathbf{x}) = \mathbf{A}^T \mathbf{x} + b \quad (2)$$

where  $\mathbf{A} \in \mathbb{R}^{3 \times 1}$  and  $b = \bar{I}$ .  $\bar{I} \in \mathbb{R}$  is the mean of the intensity values of the points in  $\mathcal{P}_I$ . Since the intensity values of points in  $\mathcal{P}_I$  are known, we can estimate  $\mathbf{A}$  by resolving the following model fit (least square) problem:

$$\arg \min_{\mathbf{A}} \sum_{i=1}^n \left\| \hat{I}(\mathbf{x}_i) - I(\mathbf{x}_i) \right\|^2 \quad (3)$$

The detailed calculation is given in our open-source code implementation. Once  $\hat{I}(\mathbf{x})$  is obtained, we can compute the 3D intensity gradients  $\nabla I \in \mathbb{R}^{3 \times 1}$  at  $\mathbf{p}_0$ . The direction of  $\nabla I$  of a given point indicates the direction where the intensity has the fastest decline and the norm,  $|\nabla I|$ , implies the rate

of descent. Inspired by LOAM [15], [38], which selects a point as a feature if its geometric curvature is larger than a threshold, we preserve the 3D point if its  $|\nabla I|$  is larger than a threshold in the downsampling procedure.

### C. Spatial Distribution Analysis of Downsampling Result

The downsampling preserves the points belonging to the outlines of objects with high intensity-contrast, such as stop signs, notices on the wall, and fiducial markers. In this section, we analyze the point cloud from the geometric perspective. The foundation of doing so is the fact that the points belonging to the fiducial markers will be isolated from those of the other objects after the downsampling (see the zoomed view of Fig. 7(a)). To explain the isolation of the points, we need to review the design of the marker's pattern as shown in Fig. 2.

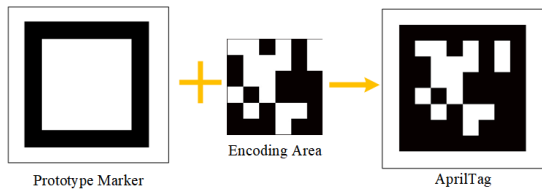


Fig. 2. A diagram to illustrate the design of a typical square fiducial marker [1]. A square fiducial marker is a combination of the prototype marker (a black frame inside a white frame) and the encoding area.

In the visual fiducial marker system, such as AprilTag [1], the aim of adopting the prototype marker (the black-white protector frame) is to isolate the marker from the environment and to construct a square shape that can be easily recognized by the visual quad detector. Despite the fact that the design of the prototype marker does not consider any factors related to LiDAR, we found that the prototype marker also brings an important benefit to this LiDAR application: the white regions of the marker naturally have higher intensity values than the black regions, and thus, the prototype marker after the downsampling is rendered as a square double-ring that isolates the points inside the coding area from the environment. We utilize this benefit to develop the followed-up pipeline. The isolation makes the points belonging to the markers spatially distinguishable from those of the other objects. Thus, we employ the method introduced in [39] to further segment the downsampling result into clusters. Each cluster is represented by an oriented bounding box (OBB) as shown in Fig. 7(b).

### D. Geometric Characteristic Analysis of Clustering Result

In this section, we analyze the geometric characteristic of each cluster to verify if it has the potential to be a LiDAR fiducial marker. Specifically, the bounding box of a cluster needs to satisfy two criteria to be recognized as a candidate that could contain a LiDAR fiducial marker. The first criterion is subject to the marker size:

$$\sqrt{2a^2 + \delta^2} \leq L_{OBB} \leq \sqrt{4a^2 + \delta^2} \quad (4)$$

where  $L_{OBB} = \sqrt{l^2 + w^2 + h^2}$  is the cuboid diagonal of the OBB with  $l$ ,  $w$ , and  $h$  ( $h \leq \delta$ ) being the length, width, and height, respectively.  $a$  denotes the side length of the marker.  $\delta$  is the trifling thickness of the marker.

The second criterion, as shown in Eq. (5), is based on the fact that the shape of the marker is square:

$$\frac{1}{1.5} \leq \frac{l}{w} \leq 1.5 \quad (5)$$

We explain these two criteria as follows. The OBB is the minimum 3D box that encloses the cluster where its sides that correspond to the length, width, and height are parallel to the first, second, and third primary components (PCs) of the feature point cluster. Moreover, the height is trivial compared to the length and width since the marker is a planar object. Thus, we neglect the height for now and consider the possible size range of the OBB in 2D space. The possible size of the OBB for a given marker is shown in Fig. 3. In light of the definition of the OBB [40], we know that  $AC \perp AE$  and  $AE \perp AF$ . In this work, we assume that the side length of the marker,  $a$ , is given. It is illustrated in Fig. 3 that  $BC = a \cos \theta$  and  $DC = a \sin \theta$ . Thus,  $AB = DC$ , such that  $AC = a(\cos \theta + \sin \theta)$ . Similarly,  $AE = EF = CF = a(\cos \theta + \sin \theta)$ . At this point, we conclude that: 1) the OBB in this case is a square; 2) the side length of the OBB is  $a(\cos \theta + \sin \theta)$ . Given that  $\theta \in [0, 2\pi]$ , we have  $a(\cos \theta + \sin \theta) \in [a, \sqrt{2}a]$ . In practice, the orientations of the first and second PCs are subject to the feature points distribution, which is determined by the unique black-and-white pattern of the marker (the encoding area as shown in Fig. 2). Although the pattern cannot be known in advance, the cases where the OBB reaches the smallest and largest sizes (see Fig. 4) are already found according to the proof above.

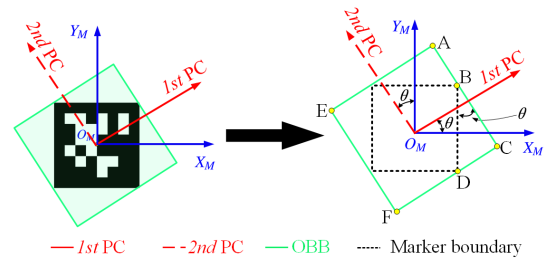


Fig. 3. A diagram of the possible OBB size for a given marker.  $O_M - X_M - Y_M$  is the marker coordinate system.  $\theta$  is the angle between the first PC and the x-axis. On account of the fact that the first PC and second PC are perpendicular to each other, the angle between the second PC and the y-axis is  $\theta$  and  $\angle DBC = \theta$  as well.

In summary, if the side length of the marker is  $a$ , the area of the 2D OBB,  $S_{OBB}$ , is in the following range:

$$a^2 \leq S_{OBB} \leq 2a^2 \quad (6)$$

Taking the marker's thickness,  $\delta$ , into consideration as well, we can obtain the first criterion as shown in Eq. (4). In addition, the OBB projection on the plane of length and width is square. Thus, Eq. (5) is adopted as the second criterion. Ideally,  $l \approx w$  since the marker is a square.

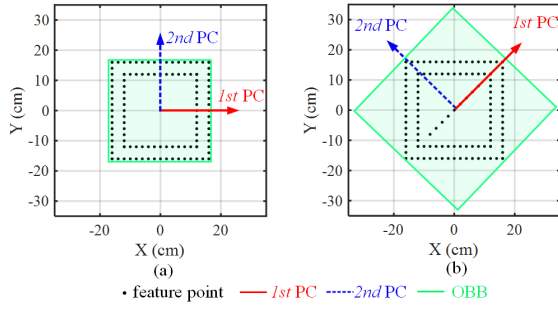


Fig. 4. A rough schematic of the smallest (a) and the largest (b) OBBs. (a):  $1st\ PC \parallel s_1$  and  $2nd\ PC \parallel s_2$  where  $s_1$  and  $s_2$  are the horizontal side and vertical sides of the marker, respectively. (b):  $1st\ PC \parallel d_1$  and  $2nd\ PC \parallel d_2$  where  $d_1$  and  $d_2$  being the two diagonals of the marker.

Whereas in the real world, the marker cannot be perfectly scanned by LiDAR, and LiDAR also has ranging noise. As a result, the shape of the OBB on the length and width plane could be distorted. Hence, we make the requirement on  $l \approx w$  less strict as shown in Eq. (5).

#### E. Marker Detection via Intermediate Plane

After analyzing the point cloud from the 3D intensity gradients and 3D geometric perspectives, we obtain the locations of objects with high intensity-contrast and shapes/sizes similar to the fiducial marker. We then inspect these locations (OBBs) in the raw point cloud. When extracting points falling into the OBBs, a buffer is adopted to extend the OBBs, preserving more regions around an OBB in case it does not completely cover the fiducial marker. This indicates that, for each OBB, the pose (position and orientation),  $\mathbf{T}_{OBB}^{-1}$ , is kept while the size is enlarged by multiplying the length, width, and height with an amplification factor,  $t_b$ . The recommended value of  $t_b$  is twice the marker's side length based on our experiment.

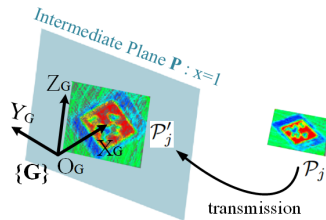


Fig. 5. An illustration of the intermediate plane.

Given that the pose of each OBB ( $\mathbf{T}_{OBB}$ ) is acquired from the analysis in Sections III-B, III-C, and III-D, we propose to eliminate the effect of occlusion by transferring the points extracted from each OBB to an intermediate plane (denoted by  $\mathbf{P}$ ) as shown in Fig. 5. The detailed transmission process is as follows. Define the point set of the  $j$ th OBB as  $\mathcal{P}_j$  and

<sup>1</sup> $\mathbf{T}_{OBB}$  denotes the transmission from the global coordinate system  $\{\mathbf{G}\}$  to the OBB frame. The OBB frame refers to a coordinate system whose X, Y, and Z axes are parallel to the length, width, and height of the bounding box. The origin of the OBB frame is located at the center of the bounding box.

a point of  $\mathcal{P}_j$  as  $\mathbf{p}_j \in \mathbb{R}^3$ .  $\mathbf{p}_j$  is first transmitted to the origin of the global coordinate system  $\{\mathbf{G}\}$  through the inverse of  $\mathbf{T}_{OBB}$ :

$$\mathbf{p}_G = \mathbf{T}_{OBB}^{-1} \cdot \mathbf{p}_j = \mathbf{R}^{-1} \cdot \mathbf{p}_j - \mathbf{R}^{-1}\mathbf{t} \quad (7)$$

where  $\mathbf{p}_G$  is the point transmitted to the origin of  $\{\mathbf{G}\}$ .  $\mathbf{T}_{OBB} = [\mathbf{R}|\mathbf{t}]$  where  $\mathbf{R}$  is the  $3 \times 3$  orthogonal rotation matrix and  $\mathbf{t}$  is the  $3 \times 1$  translation vector. After transmitting all the points in  $\mathcal{P}_j$  using Eq. (7), we obtain a new point set  $\mathcal{P}_j^G$ . Then, all points belonging to  $\mathcal{P}_j^G$  are transferred to the intermediate plane  $\mathbf{P}$ :

$$\mathbf{p}'_j = \mathbf{T}_{in} \cdot \mathbf{p}_G = \mathbf{R}_{in} \cdot \mathbf{p}_G + \mathbf{t}_{in} \quad (8)$$

where  $\mathbf{p}'_j$  is the point transmitted to the intermediate plane.  $\mathbf{T}_{in} = [\mathbf{R}_{in}|\mathbf{t}_{in}]$  where  $\mathbf{R}_{in} = \mathbf{I}_{3 \times 3}$  is an identity matrix and  $\mathbf{t}_{in} = [1m, 0, 0]^T$  since the plane equation is  $x = 1m$ . Define the point set on the intermediate plane as  $\mathcal{P}'_j$ . Given that  $\mathcal{P}'_j$  is a point cloud with no occlusions, marker detection in it is straightforward following the preliminary method introduced in Section III-A. Define the point set composed of the detected 3D fiducials as  $\mathcal{F}_j$ . If the set  $\mathcal{F}_j$  exists, we can transmit the points in  $\mathcal{F}_j$  from the intermediate plane back to their original locations using the reverse processes of Eqs. (7-8).

## IV. EXPERIMENTAL RESULTS

In this section, we present experimental results comparing the proposed approach to existing LiDAR fiducial marker systems, including IILFM [20], LiDARTag [17], and A4LiDARTag [21]. In Section IV-A, we test the approaches on both synthesis and real-world point clouds to demonstrate that only our method is applicable to a point cloud with occlusion. In Section IV-B, we demonstrate quantitatively that our method has better pose estimation accuracy.

### A. Qualitative Evaluation

We first compare the existing methods [20], [17], [21] with our approach on a synthesis point cloud (see Fig. 6), which is a stitch of two subpoint clouds. We want to use this simple scene to explicitly present the visual results of the main steps of the proposed method. Then, we compare the approaches on the real-world 3D map shown in Fig. 1. The visual results after completing the major steps of the proposed approach are shown in Fig. 7 and Fig. 8. Please refer to the caption for details.

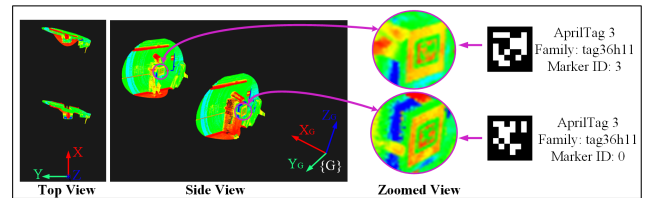


Fig. 6. A synthesis point cloud with occlusion. The two presenters are holding two different AprilTag markers [1]. As illustrated in the top view, observing along the X-axis of the global coordinate system  $\{\mathbf{G}\}$ , the back subpoint cloud is totally blocked by the front one. Thus, it is infeasible to project the 3D point cloud to a 2D image plane due to the occlusion.



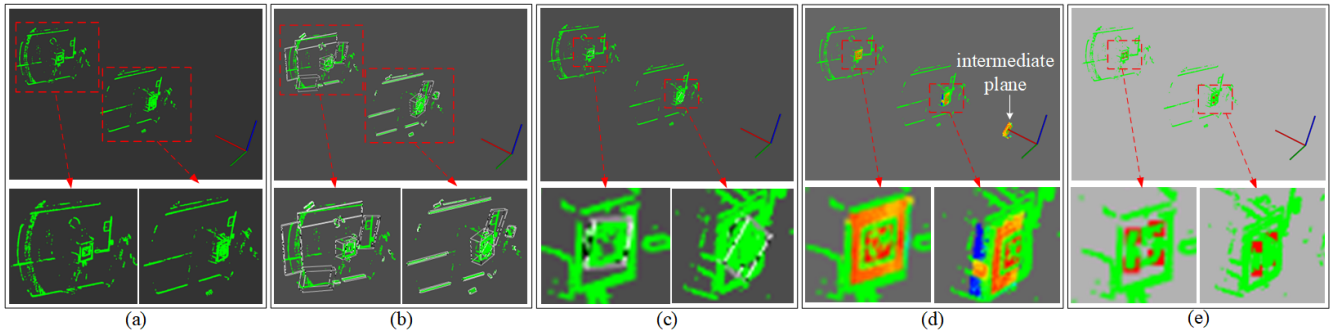


Fig. 7. Visual results of the main steps. The raw point cloud is shown in Fig. 6. (a): The point cloud after downsampling using 3D intensity gradients. (b): Clustering of the downsampling result. Each cluster is labeled with an OBB. (c): Preserved OBBs according to the proposed criterion. (d): Points extracted from the raw point cloud and the points transmitted to the intermediate plane. (e): LiDAR fiducial markers detection result. The detected vertices are rendered in red.

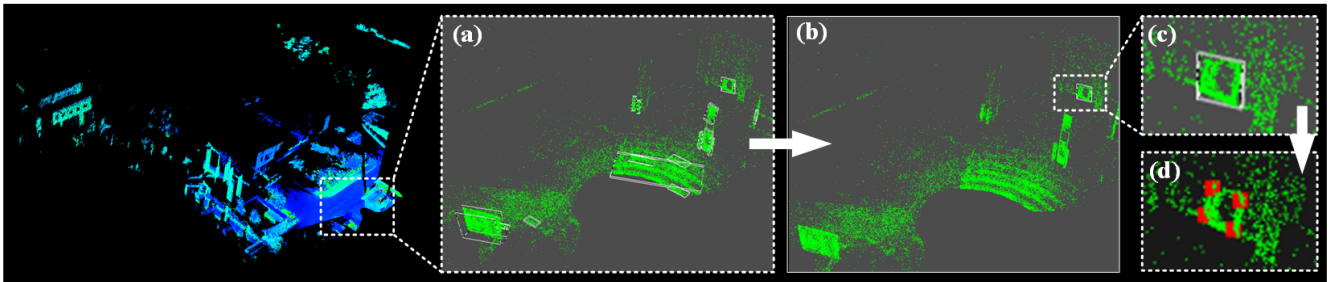


Fig. 8. An illustration of the marker detection process on the 3D map built from SLAM. (a): The result after conducting downsampling and clustering. (b): The result after adopting the proposed geometric criterion. As seen, all the clusters but the one belonging to the marker are filtered out. (c): The zoomed view of the preserved OBB. (d): A zoomed view of the detected 3D fiducials, which are rendered in red.

TABLE I

COMPARISON WITH THE PREVIOUS METHODS ON GENERAL POINT CLOUDS. GT REFERS TO GROUND TRUTH. NUM DENOTES THE NUMBER OF LiDAR FIDUCIAL MARKERS.

Scene	GT Num	Method	Detected Num
Fig. 6	2	LiDARTag [17]	0
		A4LiDARTag [21]	0
		IILFM [20]	1
		<b>Ours</b>	<b>2</b>
Fig. 1	1	LiDARTag [17]	0
		A4LiDARTag [21]	0
		IILFM [20]	0
		<b>Ours</b>	<b>1</b>

The summary of the qualitative evaluation is presented in Table I. As seen in the Table, only the proposed approach successfully detects all the fiducials in the two scenes. We take the point cloud shown in Fig. 6 as an example to analyze the reasons for the detection failures of the existing methods. LiDARTag [17] supports patterns from AprilTag3 [1], however, it requires adequate clearance around the markers. In our scenes, markers are papers attached to other planes with no clearance. A4LiDARTag [21] proposes to utilize the range image to detect fiducials. Whereas, as shown in the range image of Fig. 9, there is no useful information in it. IILFM [20] projects the raw point cloud onto the image plane directly. Thus, only the marker in the front point cloud is

preserved in the intensity image due to occlusion (see the intensity image in Fig. 9). Therefore, only one marker is detected. By contrast, our approach generates an intensity image for each location that could contain a fiducial marker. Thus, as shown in Fig. 9, each marker is preserved in its corresponding intensity image.

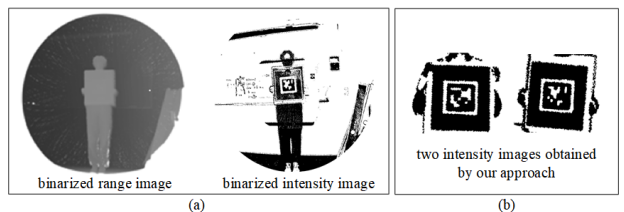


Fig. 9. (a): The 2D intensity/range images after projecting the 3D point cloud shown in Fig. 6 onto the 2D image plane. (b): The intensity images obtained through our approach from the point cloud shown in Fig. 6.

### B. Quantitative Evaluation

In this section, we conduct experiments introduced in Fig. 10 to demonstrate that the proposed method has better pose estimation accuracy. Since we want to compare our method with other approaches in terms of pose estimation accuracy, it is necessary to use this occlusion-free scene because other approaches are not applicable to point clouds with occlusion. We test the methods under different distances from the LiDAR to the fiducial marker. Unfortunately, LiDARTag [17]

TABLE II

COMPARISON OF OUR APPROACH, IILFM [20], AND APRILTAG3 [1] WITH RESPECT TO POSE ESTIMATION ACCURACY. THE DISTANCE REFERS TO THE DISTANCE FROM THE FIDUCIAL MARKER TO THE LiDAR.

Distance	Method	X error (m)	Y error (m)	Z error (m)	Roll error (deg)	Pitch error (deg)	Yaw error (deg)
2m	AprilTag3 [1]	0.016	0.034	0.016	0.807	3.166	1.244
	IILFM [20]	0.003	0.006	0.017	0.423	0.457	0.399
	<b>Ours</b>	<b>0.002</b>	<b>0.005</b>	<b>0.011</b>	<b>0.315</b>	<b>0.305</b>	<b>0.391</b>
3m	AprilTag3 [1]	0.058	0.124	0.044	1.369	7.963	2.904
	IILFM [20]	0.026	0.021	0.093	0.930	1.182	0.859
	<b>Ours</b>	<b>0.006</b>	<b>0.009</b>	<b>0.015</b>	<b>0.343</b>	<b>0.322</b>	<b>0.455</b>
4m	AprilTag3 [1]	0.072	0.407	0.233	1.433	9.292	13.343
	IILFM [20]	0.024	0.024	0.107	0.342	2.020	1.111
	<b>Ours</b>	<b>0.008</b>	<b>0.014</b>	<b>0.016</b>	<b>0.302</b>	<b>0.389</b>	<b>0.478</b>



Fig. 10. The experimental setup for quantitative evaluation. The LiDAR model is Livox MID-40. A Letter size AprilTag is put on the wall. The OptiTrack system provides the ground truth of the 6-DOF LiDAR pose.

and A4LiDARTag [21] fail to detect the marker, and thus, we compare the proposed approach with IILFM [20] and the widely-used visual fiducial marker system, AprilTag3 [1]. Note that when testing AprilTag3, the adopted sensor is a camera. As shown in Table II, both the accuracy of IILFM and AprilTag3 degrades as the distance from the sensor to the marker increases while the accuracy degradation of IILFM is less severe compared to AprilTag3. The accuracy of the proposed approach is slightly better than IILFM at a distance of 2m. However, unlike IILFM, our approach maintains a decent accuracy when the distance increases.

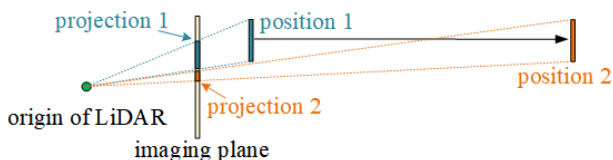


Fig. 11. An illustration of the negative correlation between the projection size and the distance. It is straightforward to prove the negative correlation using the similarity of triangles.

The analysis of the result is given as follows. Suppose that both IILFM [20] and our approach are employed to process the same point cloud where the distance from the fiducial marker to the LiDAR is 3m. IILFM [20] projects the entire raw point cloud to the image plane directly without any analysis. By contrast, our approach first transforms the points potentially corresponding to the marker to the intermediate plane and then projects them to the image plane. Based on the negative correlation between the projection size and distance,

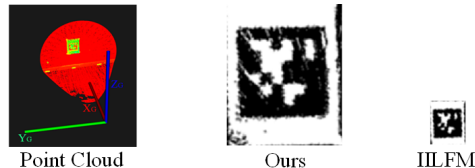


Fig. 12. The visual comparison of the intensity images obtained by our method and IILFM [20] from the same point cloud (shown on the right side) when the distance from the marker to the LiDAR is 3m.

as illustrated in Fig. 11, our method results in a larger marker projection on the image plane than IILFM [20]. The visual comparison is given in Fig. 12. Apparently, using our approach, the intensity image has fewer points overlapping and thus retains more information. This is favorable for pose estimation as it leads to more accurate observations.

## V. CONCLUSIONS

In this work, we propose a novel occlusion-resistant LiDAR fiducial marker detection method. Despite the existence of previous LiDAR fiducial marker detection methods [20], [17], [21], our method is the first that can detect the LiDAR fiducial markers in a point cloud with occlusion and return their poses with respect to the global frame. Qualitative and quantitative experiments are presented to demonstrate the superiority of the proposed approach over the existing methods.

## ACKNOWLEDGMENT

The authors would like to thank Yicong Fu, Guile Wu, Han Wang, Brian Lynch, Yuan Ren, Shuo Zhang, Marc Savoie, and Shiyuan Jia for insightful discussions.

## REFERENCES

- [1] M. Krogius, A. Haggemiller, and E. Olson, "Flexible layouts for fiducial tags," in *Proc. IEEE/RSJ International Conference on Intelligent Robots and Systems*, 2019, pp. 1898–1903.
- [2] F. J. Romero-Ramirez, R. Muñoz-Salinas, and R. Medina-Carnicer, "Speeded up detection of squared fiducial markers," *Image and vision Computing*, vol. 76, pp. 38–47, 2018.
- [3] L. Calvet, P. Gurdjos, C. Griwodz, and S. Gasparini, "Detection and Accurate Localization of Circular Fiducials under Highly Challenging Conditions," in *Proc. 2016 IEEE Conference on Computer Vision and Pattern Recognition*, 2016, pp. 562 – 570.

- [4] R. Muñoz-Salinas, M. J. Marin-Jimenez, and R. Medina-Carnicer, "Spm-slam: Simultaneous localization and mapping with squared planar markers," *Pattern Recognition*, vol. 86, pp. 156–171, 2019.
- [5] S. Zhang, J. Shan, and Y. Liu, "Variational bayesian estimator for mobile robot localization with unknown noise covariance," *IEEE/ASME Transactions on Mechatronics*, pp. 1–9, 2022.
- [6] X. Liu, H. Madhusudanan, W. Chen, D. Li, J. Ge, C. Ru, and Y. Sun, "Fast eye-in-hand 3-d scanner-robot calibration for low stitching errors," *IEEE Transactions on Industrial Electronics*, vol. 68, no. 9, pp. 8422–8432, 2021.
- [7] Y. Liu, H. Schofield, and J. Shan, "Navigation of a self-driving vehicle using one fiducial marker," in *Proc. IEEE International Conference on Multisensor Fusion and Integration for Intelligent Systems*, 2021, pp. 1–6.
- [8] L. Zhang, F. Deng, J. Chen, Y. Bi, S. K. Phang, X. Chen, and B. M. Chen, "Vision-based target three-dimensional geolocation using unmanned aerial vehicles," *IEEE Transactions on Industrial Electronics*, vol. 65, no. 10, pp. 8052–8061, 2018.
- [9] J. Lin, Z. Miao, H. Zhong, W. Peng, Y. Wang, and R. Fierro, "Adaptive image-based leader–follower formation control of mobile robots with visibility constraints," *IEEE Transactions on Industrial Electronics*, vol. 68, no. 7, pp. 6010–6019, 2021.
- [10] Y. Wang, M. Shan, Y. Yue, and D. Wang, "Autonomous target docking of nonholonomic mobile robots using relative pose measurements," *IEEE Transactions on Industrial Electronics*, vol. 68, no. 8, pp. 7233–7243, 2021.
- [11] Y. Zhu, C. Yang, Z. Tu, Y. Ling, and Y. Chen, "A haptic shared control architecture for tracking of a moving object," *IEEE Transactions on Industrial Electronics*, vol. 70, no. 5, pp. 5034–5043, 2023.
- [12] L. Zheng, H. Wu, L. Yang, Y. Lao, Q. Lin, and R. Yang, "A novel respiratory follow-up robotic system for thoracic-abdominal puncture," *IEEE Transactions on Industrial Electronics*, vol. 68, no. 3, pp. 2368–2378, 2021.
- [13] D. Avola, L. Cinque, G. L. Foresti, C. Mercuri, and D. Pannone, "A practical framework for the development of augmented reality applications by using aruco markers," in *Proc. International Conference on Pattern Recognition Applications and Methods*, vol. 2, 2016, pp. 645–654.
- [14] Livox, "Livox Mapping: A mapping package for livox lidars," [online] [https://github.com/Livox-SDK/livox\\_mapping](https://github.com/Livox-SDK/livox_mapping).
- [15] J. Lin and F. Zhang, "Loam livox: A fast, robust, high-precision lidar odometry and mapping package for lidars of small fov," in *Proc. IEEE International Conference on Robotics and Automation*, 2020, pp. 3126–3131.
- [16] J.-K. Huang and J. W. Grizzle, "Improvements to target-based 3d lidar to camera calibration," *IEEE Access*, vol. 8, pp. 134 101–134 110, 2020.
- [17] J.-K. Huang, S. Wang, M. Ghaffari, and J. W. Grizzle, "Lidartag: A real-time fiducial tag system for point clouds," *IEEE Robotics and Automation Letters*, vol. 6, no. 3, pp. 4875–4882, 2021.
- [18] K. Koide, S. Oishi, M. Yokozuka, and A. Banno, "Scalable fiducial tag localization on a 3d prior map via graph-theoretic global tag-map registration," in *Proc. of IEEE/RSJ International Conference on Intelligent Robots and Systems*, 2022, pp. 5347–5353.
- [19] Y. Huang, J. Zhao, X. He, S. Zhang, and T. Feng, "Vision-based semantic mapping and localization for autonomous indoor parking," in *Proc. of IEEE Intelligent Vehicles Symposium*, 2018, pp. 636–641.
- [20] Y. Liu, H. Schofield, and J. Shan, "Intensity image-based lidar fiducial marker system," *IEEE Robotics and Automation Letters*, vol. 7, no. 3, pp. 6542–6549, 2022.
- [21] Y. Xie, L. Deng, T. Sun, Y. Fu, J. Li, X. Cui, H. Yin, S. Deng, J. Xiao, and B. Chen, "A4lidartag: Depth-based fiducial marker for extrinsic calibration of solid-state lidar and camera," *IEEE Robotics and Automation Letters*, vol. 7, no. 3, pp. 6487–6494, 2022.
- [22] A. D. Sappa and M. Devy, "Fast range image segmentation by an edge detection strategy," in *Proc. International Conference on 3-D Digital Imaging and Modeling*, 2001, pp. 292–299.
- [23] K. Koster and M. Spann, "Mir: An approach to robust clustering-application to range image segmentation," *IEEE Transactions on Pattern Analysis and Machine Intelligence*, vol. 22, no. 5, pp. 430–444, 2000.
- [24] J. M. Biosca and J. L. Lerma, "Unsupervised robust planar segmentation of terrestrial laser scanner point clouds based on fuzzy clustering methods," *ISPRS Journal of Photogrammetry and Remote Sensing*, vol. 63, no. 1, pp. 84–98, 2008.
- [25] M. A. Fischler and R. C. Bolles, "Random sample consensus: a paradigm for model fitting with applications to image analysis and automated cartography," *Communications of the ACM*, vol. 24, no. 6, pp. 381–395, 1981.
- [26] S. C. Johnson, "Hierarchical clustering schemes," *Psychometrika*, vol. 32, no. 3, pp. 241–254, 1967.
- [27] L. Fan, X. Xiong, F. Wang, N. Wang, and Z. Zhang, "Rangedet: In defense of range view for lidar-based 3d object detection," in *Proc. IEEE/CVF International Conference on Computer Vision*, 2021.
- [28] P. Kovese, "Good colour maps: How to design them," *arXiv preprint arXiv:1509.03700*, 2015.
- [29] Y. Liu. Modified Livox Mapping. (2022). [Online]. Available: [https://github.com/York-SDCNLab/m\\_livox\\_mapping](https://github.com/York-SDCNLab/m_livox_mapping)
- [30] Livox-SDK. Livox Mapping. (2020). [Online]. Available: [https://github.com/Livox-SDK/livox\\_mapping](https://github.com/Livox-SDK/livox_mapping)
- [31] G. P. Meyer, A. Laddha, E. Kee, C. Vallespi-Gonzalez, and C. K. Wellington, "Lasernet: An efficient probabilistic 3d object detector for autonomous driving," in *Proc. IEEE/CVF Conference on Computer Vision and Pattern Recognition*, 2019, pp. 12 677–12 686.
- [32] J. Mao, Y. Xue, M. Niu, H. Bai, J. Feng, X. Liang, H. Xu, and C. Xu, "Voxel transformer for 3d object detection," in *Proc. the IEEE/CVF International Conference on Computer Vision*, 2021, pp. 3164–3173.
- [33] Y. Chen, Y. Li, X. Zhang, J. Sun, and J. Jia, "Focal sparse convolutional networks for 3d object detection," in *Proc. IEEE/CVF Conference on Computer Vision and Pattern Recognition*, 2022, pp. 5428–5437.
- [34] Y. Chen, J. Liu, X. Zhang, X. Qi, and J. Jia, "Voxelnext: Fully sparse voxelnet for 3d object detection and tracking," in *Proc. IEEE/CVF Conference on Computer Vision and Pattern Recognition*, 2023, pp. 21 674–21 683.
- [35] J. Beltrán, C. Guindel, A. de la Escalera, and F. García, "Automatic extrinsic calibration method for lidar and camera sensor setups," *IEEE Transactions on Intelligent Transportation Systems*, vol. 23, no. 10, pp. 17 677–17 689, 2022.
- [36] L. Tao, L. Pei, T. Li, D. Zou, Q. Wu, and S. Xia, "Cpi: Lidar-camera extrinsic calibration based on feature points with reflection intensity," in *Spatial Data and Intelligence: First International Conference, SpatialDI 2020, Virtual Event, May 8–9, 2020, Proceedings 1*. Springer, 2021, pp. 281–290.
- [37] K. Koide, S. Oishi, M. Yokozuka, and A. Banno, "General, single-shot, target-less, and automatic lidar-camera extrinsic calibration toolbox," *arXiv preprint arXiv:2302.05094*, 2023.
- [38] J. Zhang and S. Singh, "Loam: Lidar odometry and mapping in real-time," in *Robotics: Science and Systems*, vol. 2, no. 9, 2014, pp. 1–9.
- [39] R. B. Rusu, "Semantic 3d object maps for everyday manipulation in human living environments," *KI-Künstliche Intelligenz*, vol. 24, no. 4, pp. 345–348, 2010.
- [40] P. Schneider and D. H. Eberly, *Geometric tools for computer graphics*. Elsevier, 2002.